

# Size-Dependent Second Virial Coefficients of Quantum Dots from Quantitative Cryogenic Electron Microscopy

J. van Rijssel,<sup>†</sup> V. F. D. Peters,<sup>†</sup> J. D. Meeldijk,<sup>‡</sup> R. J. Kortschot,<sup>†</sup> R. J. A. van Dijk-Moes,<sup>§</sup> A. V. Petukhov,<sup>†</sup> B. H. Erne,<sup>†</sup> and A. P. Philipse<sup>\*,†</sup>

<sup>†</sup>Van 't Hoff Laboratory for Physical and Colloid Chemistry, Debye Institute, Utrecht University, Padualaan 8, 3584 CH Utrecht, The Netherlands

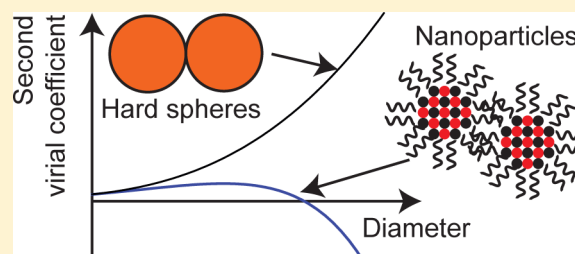
<sup>‡</sup>Electron Microscopy, Utrecht University, Padualaan 8, 3584 CH Utrecht, The Netherlands

<sup>§</sup>Condensed Matter and Interfaces, Debye Institute, Utrecht University, Princetonplein 1, 3584 CC, Utrecht, The Netherlands

## S Supporting Information

**ABSTRACT:** Cryogenic transmission electron microscopy (cryo-TEM) is utilized to determine the second virial coefficient of osmotic pressure of PbSe quantum dots (QDs) dispersed in apolar liquid. Cryo-TEM images from vitrified samples provide snapshots of the equilibrium distribution of the particles. These snapshots yield radial distribution functions from which second virial coefficients are calculated, which agree with second virial coefficients determined with analytical centrifugation and small-angle X-ray scattering. The size dependence of the second virial coefficient points to an interparticle interaction that is proportional to the QD surface area.

A plausible cause for this attraction is the interaction between the surface ions on adjacent QDs.



## INTRODUCTION

An important parameter to quantify and to compare molecular and colloidal interactions is the second virial coefficient of osmotic pressure,  $B_2$ .<sup>1</sup> It describes the first-order correction to the ideal gas equation of state and provides a link between the microscopic properties of a thermodynamic system, such as particle positions and interactions, and the macroscopic properties of this system, such as pressure. For instance, the second virial coefficient is used to predict crystallization of proteins,<sup>2</sup> necessary for the determination of their atomic structure. The second virial coefficient also plays a role in describing the steric repulsion of polymer brushes,<sup>3</sup> utilized in the stabilization of colloids, or in quantifying the interactions between these colloids.<sup>4–6</sup> Furthermore, the second virial coefficient can be used to predict the critical temperature of a liquid–gas transition according to the Vliegenthart–Lekkerkerker criterion.<sup>7</sup>

Several methods are employed to measure  $B_2$  experimentally, based on different thermodynamic connections between microscopic and macroscopic properties of the system. A well-known approach to measure  $B_2$  is angle-dependent scattering of light or X-rays, where the second virial coefficient can be obtained from the concentration dependence of the scattering intensity in the limit of forward scattering.<sup>1</sup> A second approach is to measure the osmotic pressure as a function of concentration, via a membrane osmometer<sup>8</sup> or by integration of a sedimentation equilibrium obtained from analytical centrifugation.<sup>4,9</sup> A third approach is quantitative microscopy, where the particle positions lead to the radial distribution function,

from which the second virial coefficient is calculated by integration. For particles that are too small to be imaged with optical microscopy, the only alternatives so far are scattering experiments or osmotic pressure measurements either via osmometry or sedimentation profiles. All these alternatives, however, are anything but straightforward: extrapolation to zero wave vector of scattering profiles and separation of structure factor and single-particle form factor are sometimes difficult procedures.<sup>10</sup> Osmotic pressures of nanoparticles in the dilute regime are too low for accurate osmometer measurements and the acquisition of sedimentation profiles is often a time-consuming enterprise, due to the long equilibration times required for nanoparticles.<sup>4</sup>

Therefore, we have explored a new alternative for the determination of  $B_2$  for nanoparticles in the form of cryogenic transmission electron microscopy (cryo-TEM). The basic idea is to determine directly the radial distribution function from real-space snapshots of the distribution of the nanoparticles after which  $B_2$  is determined via integration of the profiles. In this paper we will demonstrate this approach for a model system of sterically stabilized PbSe nanoparticles dispersed in the apolar solvent decalin. The  $B_2$  from cryo-TEM will be compared to values obtained from scattering and sedimentation experiments. An important issue is the particle size dependence of  $B_2$  of the PbSe quantum dots (QDs) which provides insight

Received: June 6, 2014

Revised: August 25, 2014

Published: August 25, 2014

into the nature of the particle interaction potential as further explained in the discussion.

## ■ EXPERIMENTAL SECTION

**Synthesis of PbSe Quantum Dots.** The PbSe QDs were synthesized according to the method described by Houtepen et al.<sup>11</sup> with slight modifications. The method is based on the co-injection of Pb and Se precursors in diphenyl ether (DPE 99%, Aldrich) at high temperature and under inert, nitrogen atmosphere. Pb precursor was prepared by dissolving 1.7 mmol of lead acetate trihydrate (99.999% Aldrich) in a mixture of 1.5 mL of oleic acid (OA, 90% Aldrich), 8 mL of trioctylphosphine (TOP, 90% Fluka), and 2 mL of DPE. This solution was heated at about 120 °C under low pressure ( $10^{-3}$  bar) for about 2 h and then purged with nitrogen at room temperature. A 1 M Se precursor was prepared by dissolving 0.31 g (3.9 mmol) of Se powder (99.999% Alfa Aesar) in 4 mL of TOP. Next, 1.7 mL of the Se precursor solution was mixed with the PbSe precursor solution and rapidly injected into a hot bath containing 10 mL of DPE at 190 °C. Soon after injection, the temperature dropped to about 140–150 °C, and the solution was kept at this temperature for 1.5–20 min, to obtain oleic acid-capped nanoparticles of which the PbSe core diameter varies from 5 to 12 nm. From now on, we refer to this core diameter when mentioning the size of the nanoparticles. The reaction was finally quenched by injecting a mixture of 20 mL of butanol (99.8% Aldrich) and 10 mL of methanol (99.8% Aldrich). Separation of the QDs and purification from unreacted species and excess surfactant were performed by two cycles of precipitation by methanol addition, centrifugation, and redispersion in toluene (99.8% Aldrich). Due to the better vitrification properties of decalin, the nanoparticles were transferred from toluene to decalin by evaporating the toluene under nitrogen flow and redispersing the particles in *cis/trans*-decalin (98% Merck).

**Cryogenic Transmission Electron Microscopy.** Cryo-TEM samples were prepared by placing 3  $\mu$ L of an approximately 0.4  $\mu$ M QD dispersion on a QuantiFoil TEM grid with 2  $\mu$ m holes. Excess fluid was removed using absorbent paper, resulting in a film with a thickness of a few particle diameters, after which the sample was vitrified using liquid nitrogen. The TEM grids were mounted into a liquid-nitrogen-cooled Gatan 626 cryo-holder, and cryo-TEM images were acquired using a Tecnai 12 electron microscope, operated at 120 keV.

From the images, the particle positions  $\mathbf{r}$  were determined with Mathematica 9 (Wolfram), and the radial distribution function  $g(r)$  was obtained for each image:

$$g(r) = \frac{1}{\rho} \left\langle \sum_{i \neq j} \delta(\mathbf{r}_i - \mathbf{r}_j - \mathbf{r}) \right\rangle_i \quad (1)$$

where  $\rho$  is the average number density of the system and  $\mathbf{r}$  is the center-to-center vector for two particles at positions  $\mathbf{r}_i$  and  $\mathbf{r}_j$ . To take into account the finite size of the images,  $g(r)$  was calculated from a histogram of all particle–particle distances normalized to that of a simulated ideal gas with the same boundary conditions as the sample.

The second virial coefficient was obtained by integrating the radial distribution function in the low-density limit:<sup>1</sup>

$$B_2 = 2\pi \int_0^\infty r^2 (1 - g(r)) dr \quad (2)$$

Direct numerical integration of the measured  $g(r)$  is obstructed by the noise that becomes important at large distances. Fitting the data with a suitable function that describes the main features of the radial distribution function reduces this problem. Different functions (see Supporting Information for examples) are used that are approximately zero for small  $r$ , have a peak at a particular distance  $r$ , and finally approach unity at large distances, such that the integral converges. The variations of  $B_2$  that arise from the choice of the exact mathematical description of the function are negligible when compared to the experimental uncertainty of the second virial coefficient estimated by analyzing various subsets of the images.

**Small Angle X-ray Scattering.** The second virial coefficient is also determined here via small-angle X-ray scattering (SAXS). The data were collected at the ESRF facility in Grenoble at the BM26 DUBBLE beamline operated at 11 keV. The detector, a Dectris Pilatus 1M, is mounted at 6.5 m from the sample aligned such that the beam is located in the bottom right corner of the detector thereby maximizing the range of detectable wave vectors ( $q$ ). The scattering patterns are calibrated using wet rat-tail collagen.

Radial scattering profiles are obtained by azimuthal averaging of the two-dimensional patterns with FIT2D software.<sup>12</sup> All scattering patterns were corrected for background scattering and sample adsorption before analysis.

The scattering intensity is factorized into the form factor, containing the intraparticle correlations, and the structure factor, containing the interparticle correlations. The structure factor is determined from the concentration dependence of the scattering pattern:

$$S_C(q) = \frac{I_C(q)/C}{I_0(q)/C_0} \quad (3)$$

where  $S_C$  is the structure factor for the sample with concentration  $C$  and  $I_C$  is the radial scattering intensity profile. The reference profile  $I_0$  is that measured at the lowest concentration  $C_0$  and contains only the form factor of the particles.

The second virial coefficient is determined from the structure factor:<sup>1</sup>

$$\lim_{q \rightarrow 0} \frac{1}{S(q)} = 1 + 2B_2\rho \quad (4)$$

The limit of the structure factor in the case of  $q \rightarrow 0$  is calculated utilizing the fact that  $S(q)$  is a linear function of  $q^2$  for small  $q$ . Data in the range  $0.3 \text{ nm}^{-1} < q < 0.5 \text{ nm}^{-1}$  are used in the extrapolation.

**Analytical Centrifugation.** Analytical centrifugation measurements were performed using a LUMiSizer with a custom-made upgrade to allow 100 days of continuous operation (LUM, Berlin) following the LUMiFuge procedure developed by Luigies et al.<sup>9</sup> For a typical measurement, a capillary of 50  $\mu$ m internal thickness and a length of 20 mm was filled to 10–15 mm with the sample containing about 2–15% v/v of the nanoparticles. These capillaries were then sealed by applying two-component epoxy glue on both ends and the sealed capillary is glued into a metal holder. This complete assembly was loaded into a standard 2 mm path length LUMiSizer cell. A typical centrifugation measurement consists of three steps. In the first step, 256 scans were recorded at 2 s intervals to acquire a low noise initial profile. Next, scans were recorded at half an hour intervals typically for 3–4 weeks, to reach sedimentation–

diffusion equilibrium. Finally the equilibrium profile was obtained, again by averaging 256 scans at 2 s intervals. The 0% and 100% transmission levels were determined internally from the transmission through the metal of the holder (0% transmission) and the liquid depleted from the nanoparticles at the end of the centrifugation procedure (100% transmission). The concentration profile was then calculated from the absorption at each height in the sample.

The osmotic pressure was obtained from integration of the concentration profile:

$$\Pi(r) = \Delta m \omega^2 \int_0^r \rho(r') r' dr' \quad (5)$$

where  $r$  is the distance to the rotor,  $\Delta m$  the buoyant mass of the particles,  $\omega$  the angular velocity, and  $\rho(r)$  the number density. For the lowest values of  $r$ , the number density cannot be obtained, or at least not very accurately, due to detection noise and therefore the osmotic pressure profile is assumed to follow the Van 't Hoff law. With this assumption of ideal behavior of the nanoparticles, their buoyant mass is derived from this part of the curve from the slope of the logarithm of the absorbance versus the square of the position.<sup>9</sup> As both the number density and the osmotic pressure are known at all heights in the sample, it is straightforward to construct the equation of state. The value for  $B_2$  is extracted by fitting the equation of state with

$$\frac{\Pi}{k_B T} = \rho + B_2 \rho^2 + B_3 \rho^3 + \dots \quad (6)$$

which includes the third virial term to account for deviations at high concentrations. To highlight the effect of the second and third virial coefficients, eq 6 can be rewritten as shown below.

$$\left( \frac{\Pi}{\rho k_B T} - 1 \right) \frac{1}{\rho} = B_2 + B_3 \rho \quad (7)$$

If the equation of state is plotted this way, the second virial coefficient is given by the  $y$ -intercept, and the third virial coefficient can be obtained from the slope.

## RESULTS

### Cryogenic Transmission Electron Microscopy.

In Figure 1, typical cryo-TEM images are shown for PbSe QDs with an average diameter of 5–11 nm. For each particle size, typically 100 images are acquired (>10 000 particles in total), and the  $g(r)$  is calculated for each image separately and then averaged weighted by the number of particles. Care is taken that no higher order peaks are present in each of the individual radial distribution functions which would signal that the low-density approximation is not valid. In Figure 2, measured radial distribution functions and the corresponding fits are shown for three representative systems of QDs with different diameters. The peak in the radial distribution function shifts to larger values with increasing nanoparticle diameter, indicating the increase of the center-to-center distance of two nanoparticles at contact. This distance is due to the size of the nanoparticle core and the repulsive capping ligands adsorbed at the surface, which keep the nanoparticles separated by a surface-to-surface distance of about 3.5 nm, corresponding to twice the length of the ligands. The increase in peak height indicates an increase in the QD interaction free energy, similar as observed in our earlier studies.<sup>13</sup> This increase in the interaction strength sets a limit to the particle size that can be studied, because for

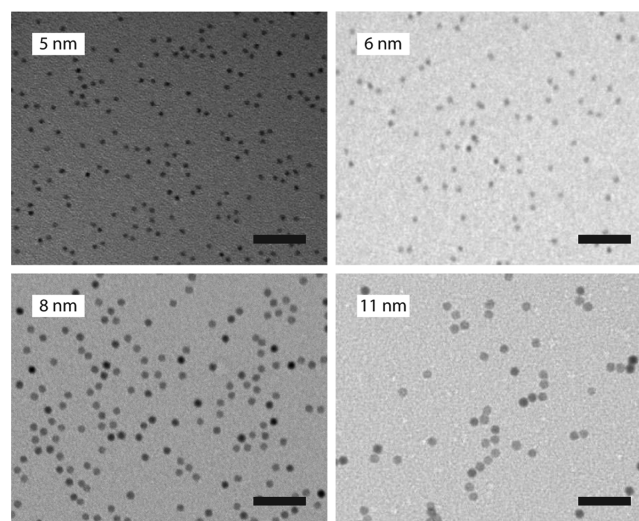


**Figure 1.** Typical cryo-TEM images of the PbSe quantum dots used in these experiments. The scale bars represent 50 nm.

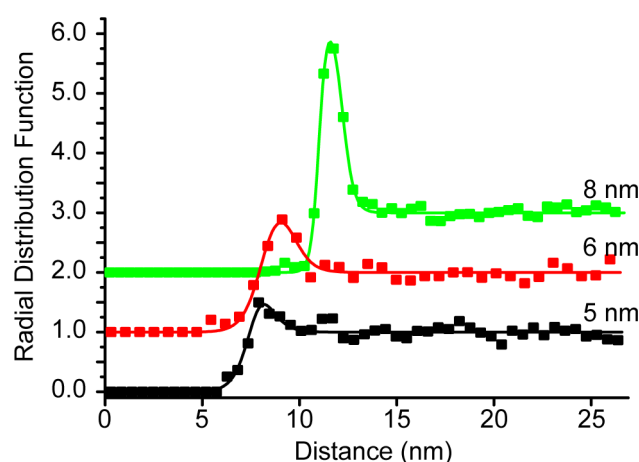


**Figure 2.** Radial distribution functions of PbSe quantum dots with diameters of 5, 6, and 8 nm. The dots are the experimental points and the solid line is a fit through the data. The curves all asymptote to 1.0 but are shifted vertically for clarity.

increasing interaction free energies, the effects of higher order particle correlations become more manifest at lower number densities. The concentrations for which the infinite dilution approximation is correct would then become so low that no sufficient statistics could be obtained on a reasonable time scale.

Integration of the fits of the radial distribution functions with eq 2 yields values of the second virial coefficient ranging from  $(1.8 \pm 2) \times 10^2 \text{ nm}^3$  for 5 nm QDs to  $(-22 \pm 2) \times 10^2 \text{ nm}^3$  in the case of 8 nm QDs (see squares in Figure 5 in the Discussion), clearly becoming more negative with increasing particle size.

**Small-Angle X-ray Scattering.** The second virial coefficient of PbSe QDs with a diameter of 4.4 and 5.7 nm are determined using SAXS for comparison with the cryo-TEM results. In Figure 3, the measured structure factors of the QDs with a diameter of 4.4 nm are plotted for different nanoparticle concentrations normalized to 1 at  $q = 1.3 \text{ nm}^{-1}$ . The structure factor shows a peak which shifts to larger  $q$  values when the concentration increases. For the highest concentrations, the center of this peak is at  $q = 0.78 \text{ nm}^{-1}$ , corresponding to a real-space distance of 8.1 nm, which for these particles corresponds



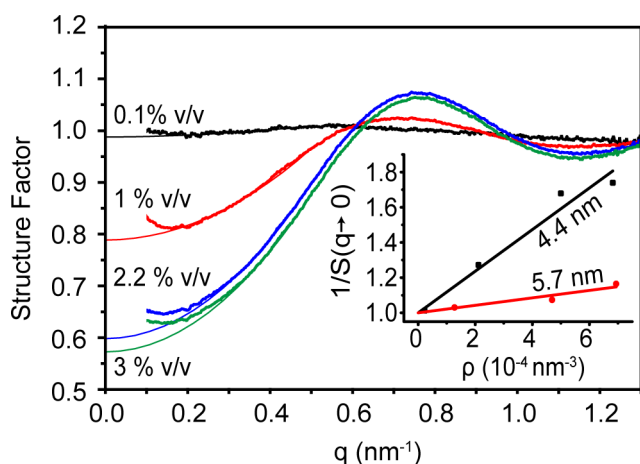


**Figure 3.** Structure factor obtained from small-angle X-ray scattering measurements. The thin lines denote the extrapolation to  $q \rightarrow 0$ . In the inset the inverse structure factor is plotted as a function of the nanoparticle concentration.

to a surface-to-surface distance of 3.7 nm. This is close to the total thickness of the capping layers on two QDs.

In the inset of Figure 3, the inverse structure factor at  $q \rightarrow 0$  is plotted as a function of concentration for two different particle sizes. According to eq 4, the inverse structure factor should be a linear function of the concentration, with a proportionality constant of  $2B_2$  and a y-intercept of 1. Fitting our data with this relation yields values of  $(6 \pm 1) \times 10^2$  and  $(1.1 \pm 0.4) \times 10^2$  nm<sup>3</sup> for the second virial coefficient of the QDs with diameters of 4.4 and 5.7 nm, respectively.

**Analytical Centrifugation.** Complementary to SAXS, the second virial coefficient is also determined from the fit of the complete equation of state determined with analytical centrifugation. In the Supporting Information, the final transmission profiles are shown as a function of the position in the capillary after 3 weeks of centrifugation at 2000 rpm ( $\sim 500$  g) for QDs with diameters of 4.4, 5.6, and 6.3 nm. The distance in the capillary is defined with respect to the center of the rotor. Experiments were also carried out for a sample of 5.3 nm QDs, but the data are not shown in the plots because they are very similar to the data of the 5.6 nm QDs.

From the logarithm of these transmission profiles, the concentration profiles are calculated, and subsequently integrated using eq 5 to calculate the osmotic pressure as a function of height. From the concentration profile and the osmotic pressure profile, the equation of state is obtained. In Figure 4, the equation of state is shown for the three particle sizes in (A) its normal representation described by eq 6 and (B) the alternative representation from eq 7. The Van 't Hoff and the Carnahan–Starling equations of state are plotted in Figure 4A as well. From Figure 4B, it becomes clear that the second virial coefficient (the y-intercept of the curves) decreases with increasing nanoparticle size, ranging from  $(0.8 \pm 0.5) \times 10^2$  nm<sup>3</sup> for the 4.4 nm particles to  $(-5.1 \pm 1.4) \times 10^2$  nm<sup>3</sup> for the 6.3 nm particles. The slope of the fits in Figure 4B is clearly nonzero, indicating that the third virial term cannot be neglected here and even higher order terms as indicated by the nonlinearity of the 4.4 nm curve. From these data we can deduce that the third virial term is always positive and goes via a minimum when the size of the nanoparticles increases, in qualitative agreement with the predictions of, for example, Elfmova et al.<sup>14</sup> for dipolar hard spheres. However, a

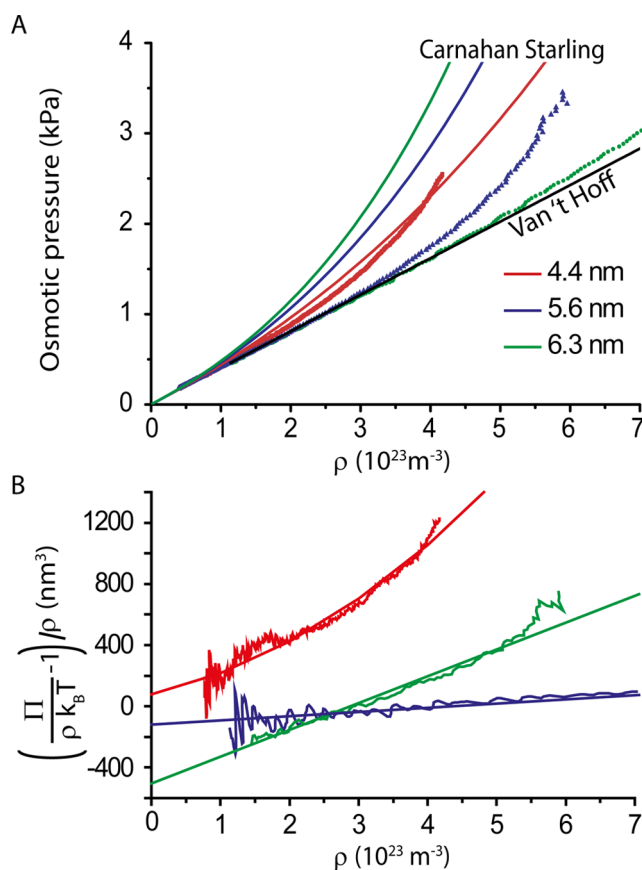


**Figure 4.** (A) Equations of state calculated from the transmission curves obtained from analytical centrifugation. In (B) a different representation is used which highlights the contributions of the second and third virial coefficients.

more systematic study is required to better quantify  $B_3$  and to interpret its size dependence.

## DISCUSSION

The second virial coefficient of the QDs clearly decreases with increasing QD diameter (Figure 5). If the interaction pair potential between the QDs is known, the second virial coefficient can be calculated using the thermodynamic equation for the second virial coefficient:

$$B_2 = 2\pi \int r^2 (1 - \exp[-U(r)/k_B T]) dr \quad (8)$$

where  $r$  is the center-to-center distance and  $k_B T$  is the thermal energy. The potential of mean force  $U(r)$  is given as the orientational average of the pair potential  $\phi$ :

$$U(r) = -k_B T \ln[\langle \exp[-\phi(r, \Omega)/k_B T] \rangle_\Omega] \quad (9)$$

$\Omega$  contains all possible orientations of two QDs. With these equations, the size dependence of the second virial coefficient can be evaluated for different interaction models and compared to the size dependence obtained from our experiments.

Before we discuss the size dependence of the second virial coefficients, we first note that all three methods give similar virial coefficients, although the  $B_2$  determined using cryo-TEM is derived from 2D images of the systems, whereas analytical centrifugation and SAXS are bulk measurements. This can be rationalized as follows: The calculation of the second virial coefficient from microscopy images is based on the assumption

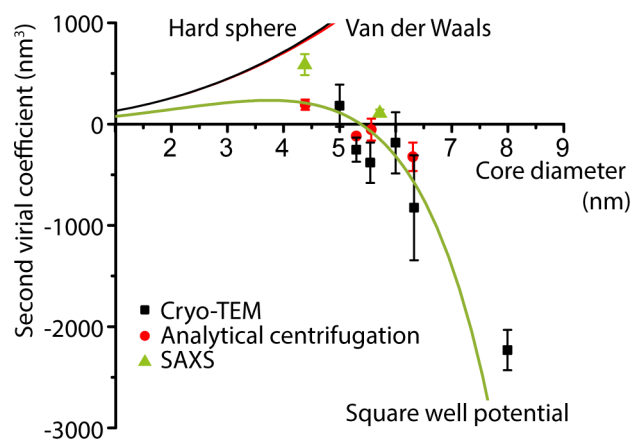


**Figure 5.** Second virial coefficient as found with the three different approaches used in this paper, plotted as a function of particle diameter. The solid lines indicate the calculated virial coefficients for hard spheres, hard spheres with a van der Waals attraction, and a square well potential. Note that the predictions for the van der Waals model are almost on top of the pure hard sphere predictions.

that the system is in the low-density limit, and the radial distribution function then becomes the exponent of the potential of mean force. Although the positions of nanoparticles are in a 2D liquid film, this does not restrict the rotational degrees of freedom of the particles, and therefore the orientational average of the pair potential is the same as that of the bulk particles and the radial distribution functions are similar for the 2D and 3D systems. If this radial distribution function is then used to calculate the 3D second virial coefficient, the results should indeed match with those determined from 3D systems directly.

We will now investigate various interaction scenarios for which the size dependence of the second virial coefficient can be predicted (see solid lines in Figure 5). The simplest interaction potential for these particles, the hard sphere interaction, predicts a continuously increasing second virial coefficient, which is much stronger than the virial coefficients measured in this work. From the hard sphere prediction, together with the fact that the virial coefficients become negative for the larger nanoparticles, we can conclude that an attractive contribution must be present in the interaction potential.

The first attractive contribution to be considered is the van der Waals force, using the Hamaker equation and a Hamaker coefficient of  $6k_B T$  for PbSe in an apolar medium.<sup>15</sup> However, the van der Waals interaction between the PbSe nanoparticles is weak, leading to an almost negligible contribution to the  $B_2$ , as shown in Figure 5. Previous experiments indicate that a dipolar interaction between the QDs might be present.<sup>13,16</sup> Recently, the magnitude of this dipole moment was determined to be 37 D for PbSe QDs with a diameter of 5.7 nm.<sup>17</sup> If we take a dipolar hard-sphere model,<sup>5,14</sup> this dipole moment would still correspond to a positive second virial coefficient on the order of  $1000 \text{ nm}^3$ . To account for the experimental second virial coefficients on the order of  $-100 \text{ nm}^3$ , the required dipole moment is about 300 D, an order of magnitude larger than reported.<sup>17</sup> Clearly, a dipolar interaction alone cannot account for the smaller and negative values of the experimental  $B_2$  values in this work.

As each of these interaction mechanisms, or combinations thereof, are insufficient to explain our experimental results,

other interaction mechanisms have to be considered. Higher order multipoles have been proposed<sup>17,18</sup> to contribute significantly to the interaction energy between the nanoparticles, which would explain the presence of strong interactions between nanoparticles<sup>13</sup> in absence of a strong dipole moment. These multipoles stem from the ionic character of the nanoparticles, which in particular becomes evident at small particle–particle separations, where the contribution of the interaction of the ions on the surface of one QD with those at the surface of another QD becomes significant. As the total interaction is likely a combination of several multipole interactions, the second virial coefficient cannot be determined uniquely as each of the terms is completely independent.

To obtain insight into the origin of the interaction between the nanoparticles, the scaling of the interaction strength with the particle diameter is an important clue. To obtain this scaling, the data are analyzed using a square well potential:

$$U(r) = \begin{cases} \infty & r < \sigma \\ -\varepsilon & \sigma \leq r < \sigma + r_w \\ 0 & \sigma + r_w \leq r \end{cases} \quad (10)$$

Here,  $\sigma$  is the diameter of the particle including the layer of capping molecules,  $\varepsilon$  the depth of the potential well, and  $r_w$  the width of the potential well. This potential captures the important requirements of the interaction potential, the repulsion at short distances and the attraction at larger separations, while the number of variables still allow a unique fit to the experiments. For this interaction potential an analytical expression for the second virial coefficient is easily obtained from eq 8:

$$B_2 = \frac{2\pi}{3}\sigma^3 + (\exp[\varepsilon/k_B T] - 1) \left( \frac{2\pi}{3}\sigma^3 - \frac{2\pi}{3}(\sigma + r_w)^3 \right) \quad (11)$$

As can be deduced from the increase of the height of the first peak of the radial distribution function in Figure 2, the strength of the interaction increases with particle size. On the other hand, the width of the peak, and thus the width of the interaction potential, has a constant value of about 2.5 nm (see Supporting Information for details); therefore,  $r_w$  is treated as a constant in this model. The depth of the potential well is modeled as a power law of the particle core diameter ( $\sigma_c$ ),  $\varepsilon = \varepsilon_0(\sigma_c/\sigma_0)^n$ , where  $\varepsilon_0$  is the potential depth of a reference system with nanoparticles with a diameter  $\sigma_0$ , and  $n$  is a scaling parameter. The total particle diameter  $\sigma$  of the square well potential is set to the core diameter plus 2.5 nm due to the presence of the capping layer, such that the center of the well corresponds to the average interparticle distance ( $\sim \sigma_c + 3.5 \text{ nm}$ ).

Fitting the experimental second virial coefficients with the above model, using  $\varepsilon_0$  and  $n$  as fitting parameters, yields a depth of the potential well of  $\varepsilon_0 = 0.5k_B T$  for QDs with a diameter of  $\sigma_0 = 5 \text{ nm}$ . Quantitative interpretation of this well depth is limited because it depends strongly on the choice of the width of the potential well. From the fit we find that the scaling parameter  $n = 2.2 \pm 0.5$ , which shows that the potential depth scales quadratically with the particle diameter, indicating that the origin of the interaction is related to the surface of the nanoparticles. This is in agreement with the proposed origin of the electric multipole interactions,<sup>17</sup> as they originate from the surface termination of a QD.

## CONCLUSIONS

The second virial coefficients of PbSe quantum dots in decalin obtained from cryogenic electron microscopy are in good agreement with those obtained from analytical centrifugation or small-angle X-ray scattering, indicating that cryo-TEM is a viable method to determine the thermodynamic properties of nanoparticle systems. A clear decrease in  $B_2$  is observed with increasing particle size due to the increasing contribution of attractive interactions. The analytical centrifugation measurements show also that the third virial coefficient is positive, as expected from theory. From a fit with a square well potential, a quadratic dependence of the interaction strength on the particle size is obtained, indicating that the interaction strength is proportional to the surface of the nanoparticles, supporting the proposed presence of electrical multipole interactions.

## ASSOCIATED CONTENT

### Supporting Information

Additional data from the centrifugation and scattering experiments. This material is available free of charge via the Internet at <http://pubs.acs.org>.

## AUTHOR INFORMATION

### Corresponding Author

\*E-mail: [a.p.philipse@uu.nl](mailto:a.p.philipse@uu.nl).

### Notes

The authors declare no competing financial interest.

## ACKNOWLEDGMENTS

This work is part of the research programme of the Foundation for Fundamental Research on Matter (FOM), which is part of the Netherlands Organisation for Scientific Research (NWO). Antara Pal and the personnel of the DUBBLE beamline are thanked for their help with the synchrotron experiment, and NWO is thanked for granting beamtime.

## REFERENCES

- (1) Vrij, A.; Tuinier, R. In *Fundamentals of Colloids and Interface Science*, Vol. IV; Lyklema, J. E., Ed.; Elsevier: Amsterdam, 2005; Chapter 5.
- (2) Neal, B. L.; Asthagiri, D.; Velev, O. D.; Lenhoff, A. M.; Kaler, E. W. Why is the Osmotic Second Virial Coefficient Related to Protein Crystallization? *J. Cryst. Growth* **1999**, *196*, 377–387.
- (3) Fischer, E. W. Elektronenmikroskopische Untersuchungen zur Stabilität von Suspensionen in Makromolekularen Lösungen. *Koll.-Zeit.* **1958**, *160*, 120–141.
- (4) Luigjes, B.; Thies-Weesie, D. M. E.; Ern , B. H.; Philipse, A. P. Sedimentation Equilibria of Ferrofluids: II. Experimental Osmotic Equations of State of Magnetite Colloids. *J. Phys.: Condens. Matter* **2012**, *24*, No. 245104.
- (5) Philipse, A. P.; Kuipers, B. W. M. Second Virial Coefficients of Dipolar Hard Spheres. *J. Phys.: Condens. Matter* **2010**, *22*, No. 325104.
- (6) Cousin, F.; Dubois, E.; Cabuil, V. Tuning the Interactions of a Magnetic Colloidal Suspension. *Phys. Rev. E* **2003**, *68*, No. 021405.
- (7) Vliegenthart, G. A.; Lekkerkerker, H. N. W. Predicting the Gas-Liquid Critical Point from the Second Virial Coefficient. *J. Chem. Phys.* **2000**, *112*, No. 5364.
- (8) Striolo, A.; Ward, J.; Prausnitz, J.; Parak, W. J.; Zanchet, D.; Gerion, D.; Milliron, D.; Alivisatos, A. P. Molecular Weight, Osmotic Second Virial Coefficient, and Extinction Coefficient of Colloidal CdSe Nanocrystals. *J. Phys. Chem. B* **2002**, *106*, 5500–5505.
- (9) Luigjes, B.; Thies-Weesie, D. M. E.; Philipse, A. P.; Ern , B. H. Sedimentation Equilibria of Ferrofluids: I. Analytical Centrifugation in

Ultrathin Glass Capillaries. *J. Phys.: Condens. Matter* **2012**, *24*, No. 245103.

(10) Philipse, A. P.; Vrij, A. Determination of Static and Dynamic Interactions Between Monodisperse, Charged Silica Spheres in an Optically Matching, Organic Solvent. *J. Chem. Phys.* **1988**, *88*, No. 6459.

(11) Houtepen, A. J.; Koole, R.; Vanmaekelbergh, D.; Meeldijk, J. D.; Hickey, S. G. The Hidden Role of Acetate in the PbSe Nanocrystal Synthesis. *J. Am. Chem. Soc.* **2006**, *128*, 6792–6793.

(12) Hammersley, A. P. FIT2D: An Introduction and Overview. ESRF Internal Report ESRF97HA02T; European Synchrotron Research Facility: Grenoble, France, 1997.

(13) van Rijssel, J.; Ern , B. H.; Meeldijk, J. D.; Casavola, M.; Vanmaekelbergh, D.; Meijerink, A.; Philipse, A. P. Enthalpy and Entropy of Nanoparticle Association from Temperature-Dependent Cryo-TEM. *Phys. Chem. Chem. Phys.* **2011**, *13*, No. 127704.

(14) Elfimova, E. A.; Ivanov, A. O.; Camp, P. J. Thermodynamics of Dipolar Hard Spheres with Low-to-Intermediate Coupling Constants. *Phys. Rev. E* **2012**, *86*, No. 021126.

(15) Talapin, D. V.; Shevchenko, E. V.; Murray, C. B.; Titov, A. V.; Kral, P. Dipole-dipole Interactions in Nanoparticle Superlattices. *Nano Lett.* **2007**, *7*, 1213–1219.

(16) Shim, M.; Guyot-Sionnest, P. Permanent Dipole Moment and Charges in Colloidal Semiconductor Quantum Dots. *J. Chem. Phys.* **1999**, *111*, No. 6955.

(17) Kortschot, R. J.; van Rijssel, J.; van Dijk-Moes, R. J. A.; Ern , B. H. Equilibrium Structures of PbSe and CdSe Colloidal Quantum Dots Detected by Dielectric Spectroscopy. *J. Phys. Chem. C* **2014**, *118*, 7185–7194.

(18) Rabani, E.; Het nyi, B.; Berne, B. J.; Brus, L. E. Electronic Properties of CdSe Nanocrystals in the Absence and Presence of a Dielectric Medium. *J. Chem. Phys.* **1999**, *110*, No. 5355.